Materials Horizons

ROYAL SOCIETY OF CHEMISTRY

COMMUNICATION

View Article Online
View Journal

Cite this: DOI: 10.1039/d5mh02158h

Received 13th November 2025,
Accepted 28th January 2026

DOI: 10.1039/d5mh02158h

rsc.li/materials-horizons

Orbital-level engineering of bonding networks to modulate halogen migration in lead-free double perovskites

Qianglong Fang,†[a] Mingao Hu,†[a] Xinying Gao,[a] Yilei Wu,[a] Qun Ji,[a] Ming-Gang Ju *[a] and Jinlan Wang [ab]

Ionic migration plays a pivotal role in determining the performance and operational stability of a wide range of optoelectronic devices. Halide double perovskites (HDPs) have emerged as promising lead-free alternatives to conventional perovskites; however, they remain susceptible to detrimental halide ion migration. Despite this, the fundamental mechanisms underlying ionic migration in HDPs are poorly understood, hindering the development of effective strategies to mitigate such instability. Here, we have redefined ion migration as a continuous bonding reconfiguration process, demonstrating that antibonding hybridization and alignment serve as precise descriptors for governing halide ion migration. Comprehensive analyses of bonding characteristics, combined with migration pathway simulations, demonstrate that engineering the B-site cations and halogens tunes the overlap of antibonding orbitals and their energetic positions relative to the Fermi level, thereby elevating the migration barrier and suppressing halide ion motion. Based on this strategy, we further construct features related to chemical bond variations and establish a machine learning (ML) framework that enables rapid prediction across the vast chemical space of HDPs. Collectively, these findings not only advance the fundamental comprehension of ionic transport in HDPs but also furnish practical design guidelines for achieving stable, lead-free perovskite optoelectronics.

New concepts

Ionic migration fundamentally governs the performance, stability, and durability of halide perovskite-based devices. Although extensive research has elucidated ion migration mechanisms in conventional lead halide perovskites, the microscopic origins in lead-free halide double perovskites (HDPs) remain poorly understood. Here, by conceptualizing ion migration as a continuous reconfiguration process of chemical bonds, we develop a unified orbital-level framework that links halide migration barriers to antibonding interactions between metals and halogens. Stronger antibonding orbital overlap and reduced energy separation from the Fermi level increase these barriers. Accordingly, we propose an orbital-level design strategy that modulates d-orbital occupancy and halogen electronegativity to suppress halide migration. Furthermore, we construct a machine learning model incorporating orbital descriptors to enable rapid prediction of migration barriers across a vast compositional landscape of HDPs. This study establishes a universal paradigm for mitigating ionic migration, paving the way for stable, high-performance, and environmentally friendly perovskite materials.

Introduction

Ionic migration is a ubiquitous phenomenon in functional materials and plays a vital role in determining the performance, stability, and reliability of a broad spectrum of energy and electronic devices.[1–4] Specifically, functional devices such as solar cells,[2] light-emitting diodes,[5] and sensors[6] are highly susceptible to ion migration under operational conditions. The migration of ionic vacancies and interstitials, triggered by electric fields, thermal effects, or applied bias, induces significant structural instabilities. These manifest as phase segregation, defect accumulation, and dynamic disorder, posing a significant challenge to long-term performance stability.[7–10] In halide perovskite optoelectronics, anion migration triggers current–voltage hysteresis and accelerated degradation, severely constraining device efficiency and stability.[11–15] These effects are not merely incidental but fundamentally linked to the metastable nature of the ionic sublattice, making ionic transport one of the primary limitations to commercial deployment of halide-based technologies.

While much progress has been made in understanding and modulating ion migration in conventional lead halide perovskites,[16–18] emerging lead-free alternatives, such as halide double perovskites (HDPs), are now drawing significant attention for their enhanced stability, environmental benignity, and structural tunability.[19–22] Nevertheless, HDPs are not immune

[a] Key Laboratory of Quantum Materials and Devices of Ministry of Education, School of Physics, Southeast University, Nanjing 211189, China. E-mail: juming@seu.edu.cn
[b] Suzhou Laboratory, Suzhou, China
† These authors contributed equally.

to the intrinsic challenges posed by mobile halide ions. Recent studies suggest that despite their different crystal frameworks, HDPs may still suffer from halide ion migration, which could similarly degrade device performance through defect formation, phase instability, or altered interfacial properties.[15,23,24] Fortunately, the structural and compositional complexity of HDPs often involves cation ordering and a wide chemical design space, which may introduce novel pathways for halide ion motion, distinct from those in conventional perovskites.

Unlike conventional perovskites, the microscopic origins and universal suppression rules of halogen transport in HDPs remain largely elusive. Which electronic and structural characteristics promote or hinder halide migration? And crucially, how can new perovskites be designed to suppress ionic mobility and retain favorable optoelectronic properties? A comprehensive understanding of the origin of halide ion migration in HDPs is essential to answer these questions. This understanding will enable the formulation of effective suppression strategies, which are critical steps toward ensuring the commercial viability of next-generation perovskite devices.

In this study, we comprehensively investigated the behavior of halide ion migration in HDPs with the general formula $A_2B_IB_{III}X_6$ by integrating first-principles calculations with molecular orbital (MO) analysis. Previous studies have mostly relied on general ideas (*e.g.*, covalency and octahedral rigidity), lacking a unified, computable standard to explain ion migration in HDPs.[25–27] In this study, we investigate the influence of local chemical bond reconstruction on halide ion migration. This enables us to propose a unified mechanism rooted in the configuration and overlap of antibonding states. Specifically, the B-site transition metal forms ionic bonds with halogens through antibonding orbital hybridization, and as the number of d electrons increases, additional electrons occupy antibonding orbitals, thereby weakening the overall bond strength. During halide ion migration, enhanced antibonding orbital overlap between the B-site cation and halogen increases the migration barrier, while cooperative lattice distortion renders direct inter-octahedral hopping energetically less favorable than edge-mediated migration. We further developed a framework integrating an ML model and these insights, which is capable of predicting the migration barrier across a wide range of the compositional space of HDPs. Specifically, HDPs identified with larger predicted migration barriers are expected to exhibit reduced ion migration phenomena in devices and suppressed halide redistribution.[28,29]

Results and discussion

An ideal HDP architecture features a three-dimensional corner-sharing octahedral network analogous to conventional ABX_3 perovskites, while exhibiting distinctive cationic ordering at the B-site. As illustrated in Fig. 1a, B_I (monovalent) and B_{III} (trivalent) cations occupy octahedral sites coordinated by six halide anions. The inherent charge disparity between B_I and B_{III} cations drives spontaneous rock-salt ordering through electrostatic stabilization, which introduces new possibilities for

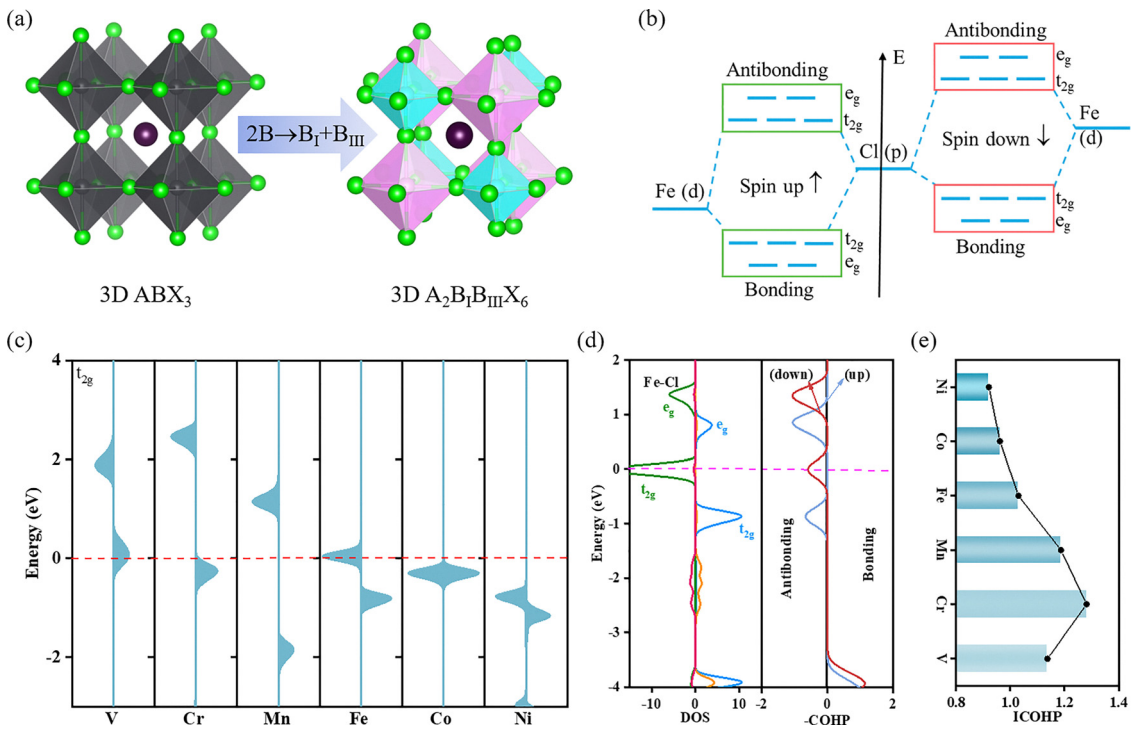

Fig. 1 (a) Schematic representation of the structures of simple and double perovskites showing the difference in the elemental composition in the B site. (b) Schematic illustration of Fe(d)–Cl(p) hybridization in Cs_2KFeCl_6 perovskite. (c) The t_{2g} orbital arrangement for different B_{III}-site 3d transition metals. (d) The DOS and COHP of the Fe–Cl bond. (e) The integrated COHP (ICOHP) of the B_{III}–Cl bond for different B_{III}-site 3d transition metals.

tailoring electronic properties through targeted cation substitution. In addition, K^+ has an optimal ionic radius ($\sim$1.38 Å) and matches the perovskite lattice well, which can minimize lattice distortion. Fe^{3+} has a $3d^5$ half-filled configuration, and its electronic state is balanced and representative, making it an ideal reference for comparative analysis with other 3d transition metals. Therefore, we employ Cs_2KFeCl_6 as a prototypical HDP to elucidate structure–property relationships. As shown in Fig. S2, the Fe 3d orbital strongly hybridizes with the Cl 3p orbital near the Fermi level, while the K 3p state is located deeper in the valence band. This electron segregation confirms that the B_{III}-site transition metal (TM) in HDP has a stronger ionic bond with the halogen, which is consistent with Pauling's electronegativity difference ($\chi_{Fe-Cl} = 1.33$ *vs.* $\chi_{K-Cl} = 2.34$). Due to the six-coordinate octahedral environment, the valence electrons of Fe rearrange, and the remaining empty orbitals participate in bonding with the lone pair of electrons of Cl, resulting in d^2sp3 hybridization (Fig. S3a). More specifically, as shown in Fig. S3b, the five 3d orbitals of Fe^{3+} split into lower-energy t_{2g} (d_{xy}, d_{yz}, d_{xz}) and higher-energy e_g (dz^2, dx^2–y^2) states under the influence of the ligand. The weak ligand field strength of Cl^- stabilizes a high-spin $t_{2g}^3e_g^2$ configuration (Fig. 1b),which is consistent with the spin state prediction of the Tanabe–Sugano plot for the d^5 system.[30]

Furthermore, we also considered different B_{III}-site TMs (V, Cr, Mn, Fe, Co, and Ni), as shown in Fig. 1c. As the number of d electrons increases, the energy separation between the spin-up and spin-down channels of the t_{2g} orbital increases, which reflects the enhanced exchange splitting caused by the high-spin configuration. From Mn to Co, the spin splitting gradually decreases. It is worth noting that Co exhibits nearly degenerate spin-up and spin-down states, implying the possible existence of a low-spin configuration. For Ni ($3d^8$), the spin polarization increases again, which may be ascribed to the enhanced inter-electron repulsion and the partial occupation of both spin channels.[31] In addition, the e_g orbital shows a consistently higher energy distribution relative to the t_{2g} orbital (Fig. S4a), which is consistent with crystal field theory. To elucidate the electron occupation and bonding strength, we further performed a crystal orbital Hamiltonian population (COHP) analysis.[32] The σ^* antibonding orbital of the Fe–Cl bond is partially filled (Fig. 1d), which reduces the bonding strength and may promote Cl^- migration through bond length fluctuations induced by Jahn–Teller distortion.[33] As the d orbital begins to fill (from V to Cr), the bonding peak dominates, and the increase of orbital overlap enhances the bonding strength (Fig. 1e). The Cr–Cl bond reaches maximum bond strength due to the half-filled t_{2g} orbital. For orbitals other than Cr, the bonding strength gradually decreases as more electrons occupy the antibonding orbital (Fig. S4b). Importantly, the abovementioned bonding mode of the d orbital of the B-site cation and the p orbital of the halogen anion is also suitable for other systems with different X-site halogens, B-site TMs, and A-site alkali metals (Fig. S5). However, due to the difference in halogen electronegativity and the number of d electrons, the antibonding orbital will shift, thereby affecting the B_{III}–X bond strength and halide ion migration.

In perovskite crystals, the movement of halide anions and A-site cations (such as MA^+ and FA^+) has been extensively studied to gain deeper insights into ion behavior in perovskite-based optoelectronics.[34–36] Furthermore, based on defect formation energies ΔE_f (Table S1), we have found that halide vacancies remain the most thermodynamically favorable intrinsic defects for ion migration in HDPs. However, HDPs involve cation ordering and a broad chemical design space, which may introduce new migration pathways for the movement of halide ions. Therefore, by elucidating the changes of bonding mode in HDPs, we aim to further investigate the migration behavior of halide ions along different migration paths and variations in bonding strength.

To begin with, different types of ions follow distinct preferred diffusion pathways, and these pathways can be altered by the presence of defects. Ames *et al.*[34] found that I^- migrates along the slightly curved edge of the PbI_6 octahedron, with the lowest activation energy. This synergistic effect of ion size and bonding strength is particularly evident in HDPs. Therefore, we propose two distinct Cl^- migration pathways in Cs_2KFeCl_6: (1) direct octahedral hopping along KCl_6^{5-} and $FeCl_6^{3-}$ segments, and (2) edge-mediated migration (Fig. 2a). The migration barriers (E_g) are adopted to describe the difficulty for an ion to move between adjacent equilibrium sites. By performing a series of climbing image nudged elastic band (CI-NEB) calculations between adjacent equivalent positions, we mapped the energy distribution of these migration mechanisms. We also compared our CI-NEB calculations with well-known Ag-based HDPs for which ion activation energies and halide migration barriers have been reported (Fig. S7). The calculated results match the experimental values well and follow the same theoretical compositional trends.[37–39]

For Cs_2KFeCl_6, the calculated E_g for the two segments of pathway 1 are 1.578 eV and 0.29 eV, respectively (Fig. 2b). This indicates that Cl^- migration around $FeCl_6^{3-}$ is much easier than that around KCl_6^{5-}, reflecting the key role of transition metal d orbitals in bonding. The energy barrier for pathway 2 is 1.995 eV, which is higher than that of pathway 1, establishing pathway 1 as the energetically favorable route. The high barrier of the direct hopping path is attributed to the fact that this process involves the cooperative deformation of multiple octahedra and the subsequent destruction of the bonding network of adjacent $FeCl_6^{3-}$ units. In contrast, the edge-mediated migration path minimizes the energy cost of structural reconstruction through localized bond reorganization. As shown in Fig. S6, the lattice distortion induced by the direct transition (pathway ① → ③) is significantly stronger than that induced by edge-mediated migration. In addition, comparative COHP analysis of the initial state (IS) and transition state (TS) demonstrates that the d–p antibonding orbital occupancy of the Fe–Cl bond increases significantly in the transition state (Fig. 2c). This dynamic change of electronic structures during the migration process stems from the disruption of the octahedral bonding network, inducing enhanced orbital hybridization. The correlation between this bonding characteristic and the migration path implies that the halogen migration barrier can

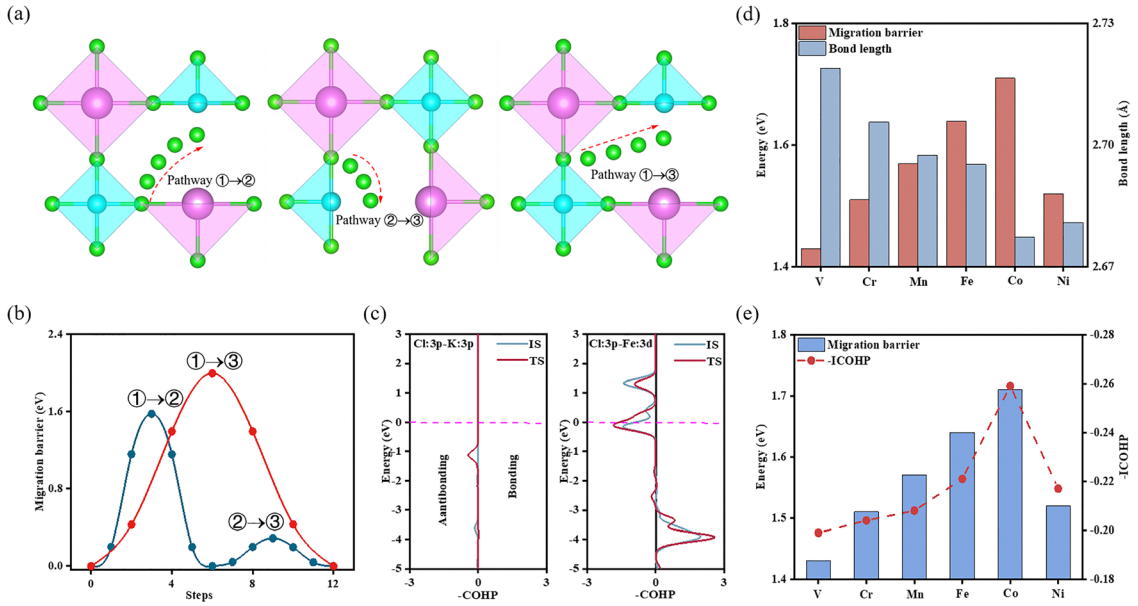

Fig. 2 (a) Schematic diagram of ion migration paths, where path 1 is divided into two parts ① → ②, ② → ③ and path 2 is ① → ③. (b) Migration barriers of Cl^- along the above two paths. (c) COHP analysis of the initial (IS) and transition states (TS) of K–Cl and Fe–Cl bonds. (d) The bond length of the TS of the K–Cl bond for different B_{III}-site 3d transition metals. (e) The ICOHP analysis of the TS of the K–Cl bond for different B_{III}-site 3d transition metals.

be directionally modulated by regulating the electronic configurations of the B-site cation (*e.g.* selecting a metal with a specific d electron configuration), providing an orbital-level design principle for inhibiting ion migration.

To further understand the effect of different B_{III}-site TMs on these migration barriers, we analyzed the local chemical environments and migration pathways around different $B_{III}Cl_6^{3-}$ octahedra. As illustrated in Fig. S8, the calculated Cl^- migration barrier associated with the KCl_6^{5-} octahedron is always higher than that of the $B_{III}Cl_6^{3-}$ octahedron. Notably, the Cl^- migration barriers in both octahedra exhibit an identical non-monotonic dependence on the TM's d-electron count, characterized by an initial increase followed by a decrease as the d-electron count increases. To elucidate this behavior, we calculated the K–Cl bond length during Cl^- migration in the KCl_6^{5-} octahedron (Fig. 2d). As the number of d electrons increases from V to Ni, the crystal field splitting leads to gradual distortions of the octahedron: in the d^3–d^6 configuration (V^{3+} to Co^{3+}), the gradually enhanced electron occupation of the t_{2g} orbital induces octahedral contraction, shortening the K–Cl bond length. The compression of the bond length increases the migration barrier by enhancing the K–Cl electrostatic interaction; after entering the d^7 region, the occupation of the e_g orbital electrons induces the Jahn–Teller distortion, resulting in axial stretching of the octahedron (the K–Cl bond length increases again) and the weakening of the bond causes the lowering of the migration barrier. The above mechanism is also applicable to Cl^- migration in the $B_{III}Cl_6^{3-}$ octahedron (Fig. S9). This non-monotonic change echoes the strain regulation mechanism in $MAPbI_3$: lattice compression inhibits ion migration by enhancing the covalency of the Pb–I bond, while tensile strain reduces the activation energy by forming defect states.[40] Additionally, our previous analysis suggests a strong correlation between the migration barrier of halide ions and the strength of anti-bonding orbitals. Hence, we also analyzed the ICOHP of the K–Cl bond for different B_{III}-site transition metals, as shown in Fig. 2e. Clearly, as the number of d electrons in the TM increases (from V to Ni), the antibonding orbitals gradually shift toward the Fermi level (Fig. S10), while the bonding strength is only slightly enhanced. This accounts for the fact that the Cl^- migration barrier primarily depends on the energy difference between the antibonding orbital energy level and the Fermi level. The anomalous behavior of the Ni system originates from the ligand field destabilization caused by its electronic configuration: the strong σ* antibonding leads to the weakening of the Ni–Cl bond (Fig. S10b), while the partial occupation of the antibonding orbital causes transient Ni–Cl bond rupture in the transition state, thereby reducing the migration barrier. This effect of orbital-configuration coupling demonstrates that, by selecting a transition metal with a specific number of d electrons (such as a d5 configuration), the octahedral rigidity and antibonding orbital distribution can be simultaneously optimized, thereby achieving precise regulation of the halogen migration barrier.

To validate the broader applicability of previous orbital design principles, we also investigated effects of different X-site halides (F, Cl, and Br) and B_I-site elements (Na, K, and Rb) (Fig. 3a and b). For X-site halides, the regulation of the migration barrier by the electronegativity of the halogen originates from the difference in the orbital hybridization pattern with the B-site metal. The substitution of F with Br at the X-sites elevates the energy level of the halogen's p orbital. This shift enhances the matching between the p orbital and the B-site d orbital, resulting in a change in the distribution of the Fe–X

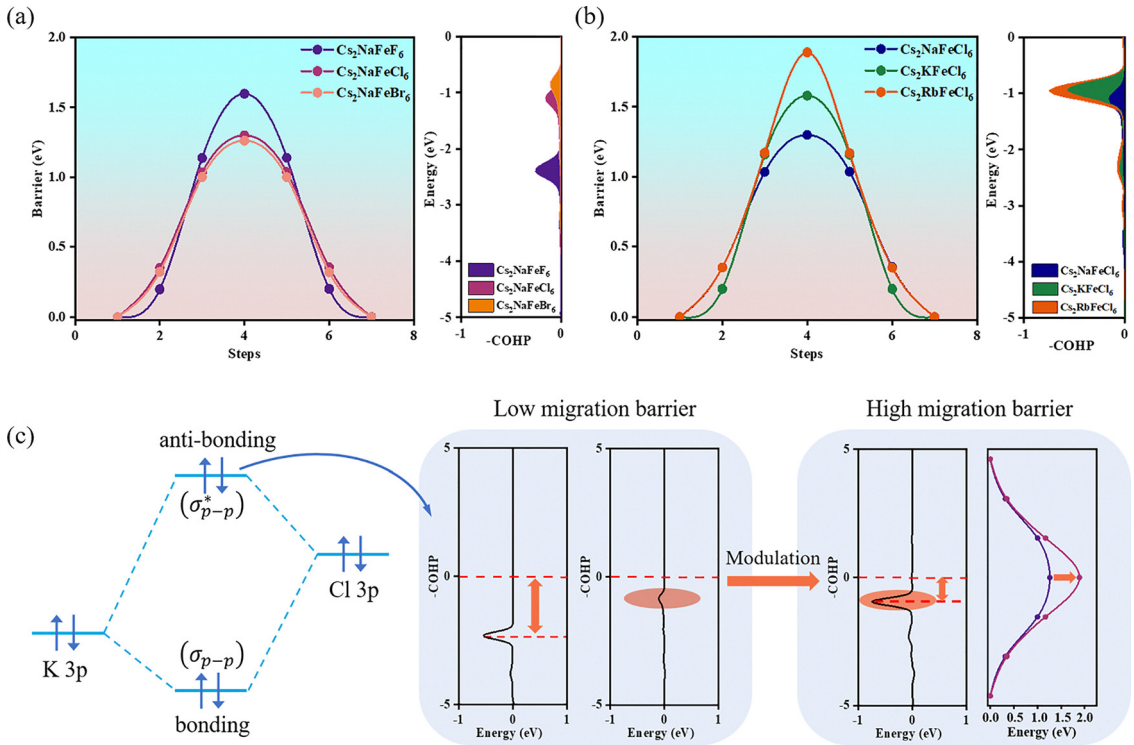

Fig. 3 (a) The migration barrier and COHP analysis with different halogen ions. (b) The migration barrier and COHP analysis of halogen ions with different BI cations. (c) A novel general mechanism linking halide ion migration barriers to anti-bonding orbitals, elucidating the origin of low migration barriers.

antibonding orbital near the Fermi level. COHP analysis shows that, compared with Cl and Br, the antibonding orbital overlap of F is stronger, whereas its antibonding peak position is far away from the Fermi level, which reduces the probability of electrons occupying the antibonding state through thermal excitation during the migration process, leading to a high migration barrier for F^- migration. In contrast, for Cl and Br systems, although their orbital overlap is weak, their antibonding peak position is closer to the Fermi level, which promotes the transient occupation of the antibonding orbital during the transition state of migration, thereby effectively reducing the migration barrier. For B_I-site elements, the increase in the ionic radius from Na^+ to Rb^+ induces lattice expansion. This structural relaxation weakens the orbital overlap between the B_I-site and the X-site, resulting in a significant decrease in the antibonding orbital intensity, while the energy gap changes very little. Based on these observations, we propose a universal mechanism linking halide ion migration barriers to antibonding orbitals (Fig. 3c). Low barriers arise from either a larger energy gap between antibonding orbital and Fermi level or weaker antibonding orbital overlap between B_I-site elements and halide anions. Strategies to enhance barriers include: (1) B-site substitution and (2) X-site doping. This mechanistic insight advances the understanding of ion migration in halide perovskites and facilitates the development of stable optoelectronic devices.

Based on our previous analysis and insights, we further employed an ML model to accurately predict ion migration barriers. Fig. 4a comprehensively illustrates this entire data-driven workflow and key outcomes. The feature engineering within this ML framework was closely integrated with prior microscopic mechanistic studies on bonding properties and electronic structure. As depicted in the initial stages of the flowchart, potential B_I, B_{III}, and X-site elements were selected from the periodic table (Fig. S11), generating 576 initial material combinations. However, not all these combinations were found to be thermodynamically stable or structurally suitable for double perovskites. To ensure dataset feasibility and reliability for subsequent modeling, stability criteria based on Goldschmidt's tolerance factor (t), the tolerance factor (τ), and the octahedral factor (μ) were applied. This systematic screening process eliminated unstable candidates and refined the initial pool into a curated dataset. Subsequently, the halide ion migration barriers for these curated materials were calculated using the computationally intensive CI-NEB method, a widely accepted technique for determining ion migration energy barriers in solids. Materials with calculated migration barriers below 0 eV or those with non-convergent NEB calculations were meticulously excluded, ultimately yielding a final, high-quality dataset of 150 double perovskite materials with reliable barrier values for ML. The dataset was randomly split into training and test sets (80% and 20%), with a fixed random seed to ensure reproducibility.

With the curated dataset, feature engineering was performed using the matminer package[41] to enhance model performance. Elemental features for the B_I, B_{III}, and X sites,

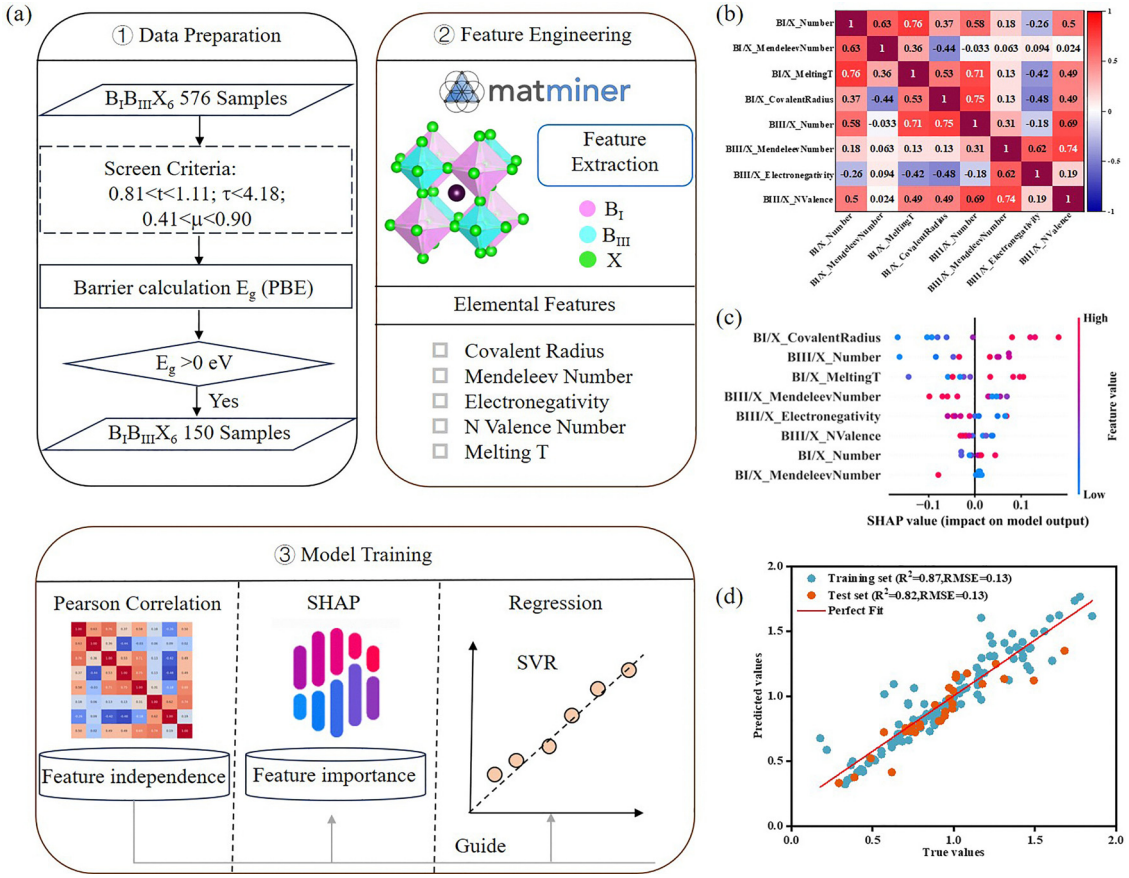

Fig. 4 (a) The flowchart for predicting the ion migration barrier with ML. (b) The Pearson correlation coefficient heatmap. (c) SHAP values for different features of the ML models. (d) Performance of the SVR model on the training and test sets.

including electronegativity, atomic radius, covalent radius, ionization energy, and electron affinity were extracted. To address unit discrepancies and scale variations, the B_I and B_{III} features were subsequently normalized with respect to the corresponding X-site. For example, the B_I/X covalent radius ratio was specifically introduced as a key physically informed descriptor. This parameter directly relates to the antibonding orbital at the transition state by quantifying the degree of orbital overlap between the B-site metal and the halogen (*e.g.*, a larger radius ratio corresponds to weaker d–p hybridization). Similarly, electronegativity was considered, as it reflects the energy level of the halogen p orbital and its influence on antibonding orbital occupation. To ensure feature independence and reduce redundancy, we performed a Pearson correlation analysis, as shown in Fig. 4b. This heatmap shows the correlations between different features, rather than the direct relationship between individual features and the migration barrier. Descriptors with high collinearity (Pearson correlation coefficient >0.9) were excluded to ensure the robustness of the subsequent ML model.

Following the feature engineering and selection phase, the predictive performance of several regression models—XGBoost, Support vector regression (SVR), random forest, linear regression, and CatBoost—on ion migration barriers was systematically assessed. As shown in Fig. S12b, XGBoost, random forest, and CatBoost exhibited significant overfitting, as evidenced by the pronounced discrepancies between their training R^2 (*e.g.*, 1.00 for XGBoost) and testing R^2 (*e.g.*, 0.72 for XGBoost) scores. This overfitting was likely attributable to their sensitivity to local electronic structure variations within the training data. The $R^2 \approx 0.68$ obtained from linear regression using the same feature set confirms that a nonlinear model is crucial for capturing the orbital-level physical mechanisms controlling ion migration. Conversely, SVR demonstrated superior balanced performance and generalization capability, establishing it as the optimal model for our limited dataset. The predictive accuracy of the optimized SVR model is explicitly demonstrated in the scatter plot of Fig. 4d, which shows strong agreement between the SVR-predicted migration barriers and the DFT-calculated actual barriers, achieving R^2 values of 0.87 on the training set and 0.82 on the test set. We also performed a 5-fold cross-validation to validate model stability (Fig. S12c). Such performance thereby validates the effectiveness of our feature engineering strategy.

To further understand the feature contributions, SHapley Additive exPlanations (SHAP) analysis[42] was employed to interpret the model and identify key influencing features. The SHAP summary plot (Fig. 4c) subsequently ranks these features, quantifying their average contribution to the SVR predictions.

Within this framework, the B_I/X covalent radius ratio was identified as the most influential descriptor. This finding is consistent with our previous mechanistic conclusion: a greater difference in covalent radii enhances the orbital overlap of the B_I–X bond, which increases the migration barrier. Meanwhile, several other descriptors like atomic number, electronegativity, and Mendeleev number also play essential roles, as they collectively capture the energy-level alignment and orbital overlap that modulate the ion migration. Furthermore, to ascertain the reliability of these feature importance rankings, bootstrap sampling stability analysis (10 iterations; Fig. S12a) was performed. The results confirmed the robustness of the key identified features, particularly the B_I–X covalent radius ratio which consistently exhibited a selection frequency of 1.0. This performance level underscores its utility for efficiently screening double perovskites with tailored ion migration.

Conclusions

In this study, we systematically investigate the electronic origins of ion migration in HDPs. We demonstrate that the migration barrier is closely linked to how chemical bonds break and reform during the process. Structurally, the formation of more stable chemical bonds between B_{III}-site TMs and halogens (*via* d^2sp^3 hybridization) hinders the breaking and reforming of bonds during ion migration, thus reducing the migration barrier. Electronically, the barrier increases with stronger B–X orbital overlap and a lower energy difference from the Fermi level. Leveraging these insights, we propose an orbital-level design strategy: modulating the d-orbital character and halogen electronegativity to suppress ion migration. Finally, we developed a machine learning model that leverages descriptors of the local chemical environment to rapidly predict migration barriers in new HDPs. A key limitation, however, is that the model was trained and validated solely on theoretical calculations from HDPs, which may constrain its accuracy when applied to other materials. Collectively, our findings establish a universal framework to understand and control ionic transport in HDPs, paving the way for the rational design of stable, high-performance perovskite-based devices.

Methods

All the DFT calculations were performed under periodic boundary conditions using the Vienna *Ab initio* Simulation Package (VASP).[43,44] To account for the van der Waals interactions between Cs and other atoms, the DFT-D3 method[45] was adopted. For all HDPs containing 3d TM cations, spin-polarized DFT calculations were employed to properly account for magnetism. A kinetic energy cutoff of 450 eV was set on a grid of $4 \times 4 \times 4$ *k*-points for perovskite. Geometry optimization was carried out under the Perdew, Burke, and Ernzerhof (PBE) exchange–correlation functional.[46] The halide anion migration energy barriers were estimated by the CI-NEB method. To simulate the halide ion migration, five images (excluding initial and final states) were linearly interpolated between the initial and final states, and the force was set to converge within 0.05 eV $Å^{-1}$ during the migration process. The spring force along the migration path was adopted during intermediate state optimization to ensure identifying the lowest energy paths. In order to gain insights into the local orbital interactions, COHP[32] analysis was performed using the LOBSTER 4.1.0 package.[47] In addition, the integrated crystal orbital Hamilton population (ICOHP) was also evaluated to quantify the strength and contributions of individual orbitals to chemical bonds. The defect formation energy ΔE_f was calculated according to $\Delta E_f = E_{deficient} - E_{perfect} + E_{vacancy}$,[38] where $E_{deficient}$ is the total energy of the structure containing the vacancy, $E_{perfect}$ is the total energy of the perfect structure, and $E_{vacancy}$ is the total energy of vacant species in a pure elemental solid or molecule.

Author contributions

M.-G. J. conceived this work. Q. F. performed DFT calculations. Q. F. and M. H. developed ML models. Q. F., M. H., M.-G. J. and J. W. analyzed the data and co-wrote the manuscript, with input from the other authors.

Conflicts of interest

The authors declare no competing interests.

Data availability

Data generated in this study and codes are available at https://github.com/mahu0124/Ion-migration. The data supporting this article, including further details on the computational methods, electronic structures and migration barriers of different HDPs, are included in the supplementary information (SI). See DOI: https://doi.org/10.1039/d5mh02158h.

Acknowledgements

This work was supported by the National Key Research and Development Program of China (grant 2021YFA1200700), the National Natural Science Foundation of China (grant 22173019). We thank the Big Data Computing Center of Southeast University and the Center for Fundamental and Interdisciplinary Sciences of Southeast University for providing the facility support for the calculations.

References

1 H. Hu, Y. Ju, J. Yu, Z. Wang, J. Pei, H.-C. Thong, J.-W. Li, B. Cai, F. Liu, Z. Han, B. Su, H.-L. Zhuang, Y. Jiang, H. Li, Q. Li, H. Zhao, B.-P. Zhang, J. Zhu and J.-F. Li, *Nat. Mater.*, 2024, **23**, 527–534.
2 Z. Shen, Q. Han, X. Luo, Y. Shen, Y. Wang, Y. Yuan, Y. Zhang, Y. Yang and L. Han, *Nat. Photonics*, 2024, **18**, 450–457.

3 Z. Zhang, W. Chen, X. Jiang, J. Cao, H. Yang, H. Chen, F. Yang, Y. Shen, H. Yang, Q. Cheng, X. Chen, X. Tang, S. Kang, X. Ou, C. J. Brabec, Y. Li and Y. Li, *Nat. Energy*, 2024, **9**, 592–601.
4 S. Gao, Z. Zhu, H. Fang, K. Feng, J. Zhong, M. Hou, Y. Guo, F. Li, W. Zhang, Z. Ma and F. Li, *Adv. Mater.*, 2024, **36**, 2311523.
5 L. Ye, Y. Gao, Y. Feng, X. Zhu, Z. Ma, D. Zhang, Y. He, H. He, Z. Ye and X. Dai, *Adv. Mater.*, 2025, **37**, 2505214.
6 L. Li, J. Pan, L. Chang, Z. Liu, G. Wu and Y. Hu, *Chem. Eng. J.*, 2024, **482**, 148988.
7 J. Wang, Y. Che, Y. Duan, Z. Liu, S. Yang, D. Xu, Z. Fang, X. Lei, Y. Li and S. (Frank) Liu, *Adv. Mater.*, 2023, **35**, 2210223.
8 L. Kong, Y. Sun, B. Zhao, K. Ji, J. Feng, J. Dong, Y. Wang, Z. Liu, S. Maqbool, Y. Li, Y. Yang, L. Dai, W. Lee, C. Cho, S. D. Stranks, R. H. Friend, N. Wang, N. C. Greenham and X. Yang, *Nature*, 2024, **631**, 73–79.
9 H. Li, Y. Feng, M. Zhu, Y. Gao, C. Fan, Q. Cui, Q. Cai, K. Yang, H. He, X. Dai, J. Huang and Z. Ye, *Nat. Nanotechnol.*, 2024, **19**, 638–645.
10 L. Song, S. Zhang, L. Duan, R. Li, Y. Xu, J. Liao, L. Sun, X. Zhou and Z. Guo, *Angew. Chem., Int. Ed.*, 2024, **63**, e202405648.
11 Z. Xiao, Y. Yuan, Y. Shao, Q. Wang, Q. Dong, C. Bi, P. Sharma, A. Gruverman and J. Huang, *Nat. Mater.*, 2015, **14**, 193–198.
12 C. Lan, H. Zou, L. Wang, M. Zhang, S. Pan, Y. Ma, Y. Qiu, Z. L. Wang and Z. Lin, *Adv. Mater.*, 2020, **32**, 2005481.
13 Y. Luo, S. Zhang, J.-S. Chen, X. Ma, K. Ma, J. Deng, Y. Jiang, L. Li, B. Lai, S. Chen, S. Wieghold and L. Dou, *Joule*, 2023, **7**, 2376–2385.
14 A. Oranskaia, J. Yin, O. M. Bakr, J.-L. Brédas and O. F. Mohammed, *J. Phys. Chem. Lett.*, 2018, **9**, 5474–5480.
15 F. Ji, J. Klarbring, F. Wang, W. Ning, L. Wang, C. Yin, J. S. M. Figueroa, C. K. Christensen, M. Etter, T. Ederth, L. Sun, S. I. Simak, I. A. Abrikosov and F. Gao, *Angew. Chem., Int. Ed.*, 2020, **59**, 15191–15194.
16 Z. Le, A. Liu, Y. Reo, S. Bai, Y.-Y. Noh and H. Zhu, *ACS Energy Lett.*, 2024, **9**, 1639–1644.
17 Y. Liang, F. Li, X. Cui, C. Stampfl, S. P. Ringer, X. Yang, J. Huang and R. Zheng, *Sci. Adv.*, 2025, **11**, eads7054.
18 T. Zhang, H. Chen, Y. Bai, S. Xiao, L. Zhu, C. Hu, Q. Xue and S. Yang, *Nano Energy*, 2016, **26**, 620–630.
19 X. Li, D. Wang, Y. Zhong, F. Jiang, D. Zhao, S. Sun, P. Lu, M. Lu, Z. Wang, Z. Wu, Y. Gao, Y. Zhang, W. W. Yu and X. Bai, *Adv. Sci.*, 2023, **10**, 2207571.
20 M. S. Uddin, M. K. Hossain, M. B. Uddin, G. F. I. Toki, M. Ouladsmane, M. H. K. Rubel, D. I. Tishkevich, P. Sasikumar, R. Haldhar and R. Pandey, *Adv. Electrode Mater.*, 2024, **10**, 2300751.
21 J. Zheng, C. Lin, C. Lin, G. Hautier, R. Guo and B. Huang, *npj Comput. Mater.*, 2024, **10**, 30.
22 Z. Rao, X. Zhao and X. Gong, *Adv. Funct. Mater.*, 2024, **34**, 2406424.
23 H. Chen, C. Li, W. Zhou, J. Wen, M. Ma, Y. Chen, K. Huang, Y. Ling, J. Wu, Y. Zhao, X. Zeng and Y. Wu, *Sol. Energy*, 2024, **284**, 113087.
24 Y. Li, H. Guo, Z. Gao, W. Yan, H. He, B. Wei, J. Sun, J. Liu, C. Lu, Y. Nakamura, W. Luo, X. Wang, B. Song and J. Hong, *Nano Lett.*, 2025, **25**, 401–409.
25 K. Liu, S. Rafique, S. F. Musolino, Z. Cai, F. Liu, X. Li, Y. Yuan, Q. Bao, Y. Yang, J. Chu, X. Peng, C. Nie, W. Yuan, S. Zhang, J. Wang, Y. Pan, H. Zhang, X. Cai, Z. Shi, C. Li, H. Wang, L. Deng, T. Hu, Y. Wang, Y. Wang, S. Chen, L. Shi, P. Ayala, J. E. Wulff, A. Yu and Y. Zhan, *Joule*, 2023, **7**, 1033–1050.
26 S. Min, M. Mukherjee, G. Szabó, P. V. Kamat and J. Cho, *Chem. Sci.*, 2025, **16**, 21950–21961.
27 Y. W. Woo, Y.-K. Jung, G. Y. Kim, S. Kim and A. Walsh, *Discover Mater.*, 2022, **2**, 8.
28 M. Pylnev, R. Nishikubo, F. Ishiwari, A. Wakamiya and A. Saeki, *Adv. Opt. Mater.*, 2024, **12**, 2401902.
29 R. Shimono, R. Nishikubo, M. Pylnev, F. Ishiwari, A. Wakamiya and A. Saeki, *ACS Appl. Energy Mater.*, 2023, **6**, 9381–9389.
30 K. V. Lamonova, E. S. Zhitlukhina, R. Y. Babkin, S. M. Orel, S. G. Ovchinnikov and Y. G. Pashkevich, *J. Phys. Chem. A*, 2011, **115**, 13596–13604.
31 W. Qu, Y. Yuan, C. Wen, J. Zhu, X. Liang, S. Chen, Z. Li, G. Cao and M. Zhang, *Energy Storage Mater.*, 2025, **75**, 103993.
32 V. L. Deringer, A. L. Tchougréeff and R. Dronskowski, *J. Phys. Chem. A*, 2011, **115**, 5461–5466.
33 R. Naheed, M. A. Zeb and K. Sabeeh, *Phys. Rev. B*, 2024, **109**, 115138.
34 C. Eames, J. M. Frost, P. R. F. Barnes, B. C. O'Regan, A. Walsh and M. S. Islam, *Nat. Commun.*, 2015, **6**, 7497.
35 J. Haruyama, K. Sodeyama, L. Han and Y. Tateyama, *J. Am. Chem. Soc.*, 2015, **137**, 10048–10051.
36 J. M. Azpiroz, E. Mosconi, J. Bisquert and F. De Angelis, *Energy Environ. Sci.*, 2015, **8**, 2118–2127.
37 M. Ghasemi, L. Zhang, J. Yun, M. Hao, D. He, P. Chen, Y. Bai, T. Lin, M. Xiao, A. Du, M. Lyu and L. Wang, *Adv. Funct. Mater.*, 2020, **30**, 2002342.
38 C. Lan, S. Zhao, J. Luo and P. Fan, *Phys. Chem. Chem. Phys.*, 2018, **20**, 24339–24344.
39 Bhawna, M. Roy, A. Kaur, A. Alam and M. Aslam, *ACS Appl. Mater. Interfaces*, 2023, **15**, 18473–18481.
40 J. Zhao, Y. Deng, H. Wei, X. Zheng, Z. Yu, Y. Shao, J. E. Shield and J. Huang, *Sci. Adv.*, 2017, **3**, eaao5616.
41 L. Ward, A. Dunn, A. Faghaninia, N. E. R. Zimmermann, S. Bajaj, Q. Wang, J. Montoya, J. Chen, K. Bystrom, M. Dylla, K. Chard, M. Asta, K. A. Persson, G. J. Snyder, I. Foster and A. Jain, *Comput. Mater. Sci.*, 2018, **152**, 60–69.
42 Y. Wu, C.-F. Wang, M.-G. Ju, Q. Jia, Q. Zhou, S. Lu, X. Gao, Y. Zhang and J. Wang, *Nat. Commun.*, 2024, **15**, 138.
43 G. Kresse and J. Furthmüller, *Comput. Mater. Sci.*, 1996, **6**, 15–50.
44 G. Kresse and J. Furthmüller, *Phys. Rev. B*, 1996, **54**, 11169–11186.
45 S. Grimme, J. Antony, S. Ehrlich and H. Krieg, *J. Chem. Phys.*, 2010, **132**, 154104.
46 J. P. Perdew, K. Burke and M. Ernzerhof, *Phys. Rev. Lett.*, 1996, **77**, 3865–3868.
47 S. Maintz, V. L. Deringer, A. L. Tchougréeff and R. Dronskowski, *J. Comput. Chem.*, 2016, **37**, 1030–1035.

